Al-Qadisiyah JournalFor Engineering Sciences 19 (2026) 001 – 010

Contents lists available at: http://qu.edu.iq

Al-Qadisiyah Journal for Engineering Sciences

Journal homepage: https://qjes.qu.edu.iq

Research Paper

Adaptive compound scaling of efficientNet via entropy estimation for chest X-ray and CT image

Nour H. Hammadah ***and Dhanesh Patel***

Department of Applied Mathematics, Faculty of Technology and Engineering The M.S. University of Baroda, Gujarat, India.

ARTICLE INFO

Article history:
Received 19 August 2025
Received in revised form 05 December 2025
Accepted 22 February 2026

keyword:
Entropy-Aware compound Scaling
EfficientNet
Chest X-ray
CT-scan
Deep Learning

ABSTRACT

Pulmonary diseases such as COVID-19, pneumonia, and tuberculosis- continue to be among the world's leading causes of death. Proper and on-time pulmonary condition classification is critical for early treatment, and this is particularly true considering the extreme heterogeneity of data in medical imaging. Although convolutional neural networks (CNNs), including EfficientNet, are powerful models for performing medical diagnosis, their single-size-fits-all approach of compound scaling is not able to accommodate variations in image complexity. In this work, we introduce Entropy Adaptive Compound Scaling (EACS), a new extension of the EfficientNet framework based on normalized Shannon entropy used as a dynamic per-image scaling cue. EACS adjusts the compound scaling factor on a per-image basis and allows the network to raise depth and width and to increase resolution for complex input instances while retaining computational speed for less complex input instances—without adjusting network architecture. EACS is assessed on two imaging modalities: chest X-rays and computed tomography (CT) scans. Our results on experiments reveal that EACS enhances COVID-19 detection accuracy from 88.07% to 90.94% on chest X-rays and elevates average accuracy on CT scans from 88.66% to 91.66% respectively. These results establish EACS as an effective, lightweight, and generalizable solution to improve diagnostic capabilities in challenging, everyday medical imaging scenarios.

1. Introduction

The increasing dependence on diagnostic imaging across global healthcare systems has significantly transformed the detection and management of diseases. With aging populations and the rising prevalence of chronic illnesses, imaging modalities such as chest radiographs (CXR) and computed tomography (CT) scans have become indispensable, particularly in respiratory medicine. However, as diagnostic demands outpace the availability of trained radiologists, automated solutions leveraging artificial intelligence (AI) have become essential for ensuring timely and accurate assessments. Lung diseases comprise various conditions that disrupt the normal functioning of the lungs, thereby affecting the overall health of the respiratory system, encompassing conditions such as asthma, tuberculosis, COVID-19, and chronic obstructive pulmonary disease (COPD); these diseases can be caused by bacterial, viral, or fungal infections, and in the United States, chronic lower respiratory diseases are among the leading causes of death [1–3]. A variety of environmental and behavioural risk factors, including air pollution, smoking, occupational exposures, and infections, contribute significantly to their burden. Given the high risk of mortality, early detection of disease is crucial to prevent progression and to enable timely medical intervention by physicians with appropriate treatment. In particular, early diagnosis of lung diseases plays a pivotal role in reducing mortality rates and improving patients' quality of life. The results of the DeepChestGNN model demonstrate how advanced artificial intelligence techniques can revolutionize the accurate and rapid detection of respiratory illnesses, thereby enhancing the chances of effective treatment and timely medical intervention [2]. The emergence of COVID-19, originating in Wuhan, China [4], and caused by the novel coronavirus SARS-CoV-2 [5], brought global attention to respiratory diseases and prompted a surge in scientific research in this field. Due to its rapid transmission and substantial mortality, the World Health Organization declared it a global public health emergency [6, 7]. As of October 16, 2020, there were 39,023,292 confirmed cases, and 1,099,586 confirmed fatalities globally [8], underscoring the severity of the pandemic and the urgent need for accurate diagnostic tools and effective clinical management. This unprecedented global health crisis accelerated the exploration of automated diagnostic solutions, thereby underscoring the importance of artificial intelligence—particularly deep learning approaches in enhancing medical imaging and clinical decision-making. Deep learning algorithms belong to neural networks, which are among the core technologies of artificial intelligence [9]. They consist of multiple convolutional layers with nonlinear activation functions, pooling layers, and fully connected layers, enabling them to capture complex patterns and textures in images, making them highly suitable for visual data interpretation applications [10]. In recent years, convolutional neural networks (CNNs) have become increasingly prominent in medical image analysis, where they are employed to classify, segment, and register diverse types of medical images such as endoscopic images, X-rays, magnetic resonance imaging (MRI), computed tomography (CT), ultrasound (US), skin images, and histopathological images—and are further utilized in the detection of diseases, including bone fractures, pneumonia, and cancer, as well as in predicting cancer progression and performing pathological classification based on genetic mutations. Convolutional neural networks (CNNs) are deep learning models that were originally developed for image recognition. They are now widely applied in medical image analysis, where they have contributed significantly to recent advances. These developments have positioned deep learning, and CNN-based approaches in particular, as state-of-the-art methods that play an important role in improving diagnostic accuracy and reliability in clinical practice [11, 12].

*Corresponding Author.
E-mail address: nour.haj-appmathphd@msubaroda.ac.in ; Tel: (+91) 873-301 7137 (Nour Hammadah)

https://doi.org/10.30772/qjes.2026.164191.1705

Nomenclature			
AI	Artificial intelligence	CCE	Categorical cross-entropy loss
CNN	Convolutional neural network	BCE	Binary cross-entropy loss
CXR	Chest X-ray	TP	True positive
CT	Computed tomography	TN	True negative
$EACS$	Entropy-aware compound scaling	FP	False positive
$FLOPs$	Floating point operations per second	FN	False negative
i	Input image (CXR or CT)	*Greek Symbols*	
L	Number of grayscale intensity levels (here L=256)	φ	Original compound scaling coefficient
$h(i)$	Histogram count of intensity level iii	φ'	Entropy-adjusted compound scaling coefficient
$p(i)$	Probability of intensity value	η	Entropy sensitivity hyperparameter
$Entropy_{norm}(x)$	Normalized entropy of the image	α	Depth scaling coefficient
$H(x)$	Shannon entropy of image	β	Width scaling coefficient
H_{max}	Maximum possible entropy	γ	Resolution scaling coefficient
H_{norm}	Normalized shannon entropy	d	Scaled network depth
AUC	Area under curve	ω	Scaled network width
ROC	Receiver operating characteristic	r	Scaled input image resolution

Deep learning networks are typically scaled by increasing one of three dimensions—depth, width, or input resolution—to improve network performance. For example, ResNet is known for its strong performance due to the increased number of layers, which makes it deeper, as demonstrated in its multiple versions such as ResNet-18, ResNet-34, ResNet-50, ResNet-101, and ResNet-152 [13, 14]. In contrast, MobileNet achieves good performance because of the increased number of channels within each layer, which makes it wider [15]. Some studies have indicated that increasing the resolution of input images can serve as an independent factor that improves the performance of convolutional neural networks, even without modifying depth or width [16]. However, this often requires an increase in model complexity. By contrast, EfficientNet achieves a balance across all three dimensions through a compound scaling method, which was used to develop a family of larger and more efficient models with reduced computational cost measured in floating-point operations per second (FLOPs). These models have demonstrated excellent performance on the ImageNet dataset [17]. Despite these advancements, current CNN models still face notable challenges, including computational inefficiencies and limited scalability, which hinder their deployment in real-time clinical settings. These issues are particularly critical in large-scale screenings, where a delicate balance between diagnostic precision and inference latency is required. Moreover, most existing approaches rely on uniform processing pipelines for all images, disregarding intrinsic variations in image complexity and thereby reducing efficiency and diagnostic accuracy. To address these limitations, we propose Entropy Adaptive Compound Scaling (EACS), an entropy-aware extension of EfficientNet. It utilizes compound scaling to balance network depth, width, and input resolution through a single scalar φ [17], achieving a strong trade-off between efficiency and accuracy. However, current implementations apply the same φ to all images, without accounting for diagnostic complexity variations.

1.1 The key contributions of our work are summarized as follows

- Entropy Adaptive Compound Scaling (EACS): A dynamic scaling strategy that adapts EfficientNet's capacity based on the entropy of each input image, enabling complexity alignment with diagnostic difficulty.
- Theoretical and Empirical Validation: Analytical justification via entropy-informed gradient analysis, supported by strong empirical results demonstrating efficiency and accuracy gains.
- Cross-Modality Benchmarking: State-of-the-art performance on publicly available CT and CXR datasets for multi-class classification of thoracic diseases.

By addressing both the performance and scalability limitations of current CNN-based medical imaging solutions, EACS represents a significant step toward clinically viable AI-assisted diagnostic systems capable of meeting the demands of modern healthcare. The remainder of this paper is organized as follows. Section 2 reviews the related work. Section 3 describes the materials and methods, including dataset details, pre-processing procedures, and the proposed Entropy-Aware Compound Scaling (EACS) approach. Section 4 presents the experimental results and discussion for two medical imaging modalities—chest X-ray and CT scan—covering baseline performance, EACS-enhanced results, and comparative analyses. Section 5 concludes the study and outlines directions for future work.

2. Related work

In recent years, the use of deep learning—especially Convolutional Neural Networks (CNNs)—has led to substantial progress in the classification of medical images by automating and enhancing the accuracy of radiographic interpretation. Among the various network architectures, EfficientNet has attracted significant interest due to its compound scaling method, which balances network depth, width, and input resolution. This approach allows for high performance with lower computational demands. This section provides a structured overview of research involving EfficientNet in medical imaging applications, with particular emphasis on thoracic disease identification, including COVID-19. Buaka and Moid (2024) [18] describe artificial intelligence as an overarching framework that includes machine learning, deep learning, and natural language processing. They emphasize its development as a transformational influence in contemporary healthcare, especially in radiology and medical imaging. This transition has reshaped clinical workflows, improved diagnostic accuracy, and laid the foundation for more responsive, data-driven patient care. Building upon these foundational insights, Jia et al. [19] and Wang et al. [20] highlighted the significant role of deep learning in advancing medical imaging, particularly in enhancing image quality and enabling disease classification. These advancements have contributed to the development of intelligent diagnostic systems aimed at streamlining clinical workflows. Nevertheless, both studies noted that detecting pneumonia from chest X-rays continues to pose challenges due to overlapping visual features and variability in radiologist interpretation. Wang et al. [21] introduced the ChestX-ray8 dataset, which includes over 100,000 chest X-ray images from more than 30,000 patients, annotated with eight thoracic disease labels. The dataset was processed using natural language processing techniques to minimize ambiguity and remove negations. Singh et al. [22] investigated the diagnostic effectiveness of deep learning in detecting abnormalities in standard chest radiographs, including temporal changes in patient status. Furthermore, another study [23] applied transfer learning with convolutional neural networks to improve pneumonia detection from chest X-ray images. Schuler et al. [23] introduced a modified EfficientNet variant, kEffNet, incorporating grouped pointwise convolutions to reduce over 84% of trainable parameters. Despite this drastic reduction, the model maintained high accuracy, especially in low-data scenarios, showing resilience against overfitting Wan et al. (ICCV 2019) [24] introduced Entropy Pooling (EP), a semantics-aware pooling mechanism that weights convolutional feature maps using Shannon entropy of localized class predictions, enabling networks to prioritize semantically important regions and improving performance in large-scale image classification and weakly-supervised semantic segmentation. Guan et al. (2025) [25] extended this concept in a different domain by proposing a lightweight 3D attention mechanism for meningioma MRI segmentation that combined entropy–curvature pooling with spatial attention modules, achieving improved parameter efficiency and segmentation accuracy. Brochet et al. (2021) [26] applied entropy at the loss function level, developing a CNN for pulmonary endomicroscopy frame classification that used a Havrda–Charvat entropy–based loss to enhance robustness against noisy inputs. While these works demonstrate that entropy can enhance CNN performance at the feature aggregation or loss optimization stages, they share a key limitation: none adapt the global network capacity—depth, width, or resolution—based on the complexity of individual images. This gap motivates our proposed Entropy-Aware Compound Scaling (EACS), which incorporates normalized image entropy directly into the scaling process, enabling EfficientNet to dynamically align its computational capacity with the diagnostic complexity of each sample. This oversight highlights a significant gap in the literature—namely, the need for architectures that can adapt their representational depth and resolution based on the visual complexity or entropy of input data. This study addresses this gap through the introduction of Entropy-Aware Compound Scaling (EACS), which incorporates entropy-guided dynamic scaling by redefining

the compound scaling coefficient as shown in Equation (1). Here, φ denotes the base scaling factor, η is a tunable hyperparameter governing entropy sensitivity, and Entropynorm [0,1] represents the normalized Shannon entropy of the input image. This formulation enables the model to allocate greater representational capacity to diagnostically complex images while conserving computational resources for simpler cases. Importantly, EACS introduces no architectural modifications to EfficientNet and incurs minimal computational overhead through fast histogram-based entropy calculations. In addition to identifying this gap, recent studies have investigated supplementary ways to enhance adaptive capacity and diagnostic performance in medical imaging models, shown by DeepBrainNet. The study [27] presents DeepBrainNet, a novel deep learning system designed to enhance accuracy and computational efficiency in the detection and classification of brain tumors from MRI images. It solves the problems of manual interpretation being slow and overfitting in small datasets by using a hybrid architecture that combines EfficientNetB0 and ResNet50 through transfer learning. EfficientNetB0 makes computations more efficient, and ResNet50's residual connections help solve the problem of the vanishing gradient. Before training on a set of 7,023 MRI images that were divided into glioma, meningioma, no tumor, and pituitary tumor, a lot of preprocessing was done. This included resizing the images, normalizing them, and enhancing them with CLAHE. DeepBrainNet did better than similar systems by getting an 88% accuracy rate for classification, an 88.75% weighted F1-score, and a 98.17% macro-AUC-ROC score. The study observes that generalization may enhance with a larger, more diverse dataset and the incorporation of multimodal imaging. Teerapittayanon et al. [28] introduces BranchyNet, a network architecture designed to balance prediction accuracy with the increased latency and energy costs of deeper neural networks during inference. By incorporating side branch classifiers and early exit points, BranchyNet allows many samples to exit the network early based on prediction confidence measured by softmax output entropy. This approach provides three main benefits: faster inference with energy savings, regularization through joint optimization of exit point loss functions, and reduced vanishing gradients by offering immediate feedback to earlier layers. BranchyNet demonstrates improved accuracy and reduced inference time across various architectures and datasets, achieving speedups of 1.5x to 5.4x on CPUs and 1.9x to 4.7x on GPUs. The architecture's adaptability for various deep learning tasks is noted, alongside limitations in optimizing branch locations and the potential integration of Meta-Recognition algorithms for tuning exit thresholds. Huang et al. [29] introduce MSDNet, a multi-scale, densely connected architecture designed to reduce computational cost and latency in image classification without compromising accuracy. By incorporating early-exit classifiers and maintaining both coarse and fine features across layers, the model adapts computation to input difficulty, allowing easy samples to be classified early. Experiments on CIFAR-10, CIFAR-100, and ImageNet show that MSDNet outperforms methods like FractalNet, ResNetMC, and DenseNetMC, achieving comparable accuracy with far fewer FLOPs. Unlike pruning or distillation approaches, MSDNet emphasizes adaptive inference efficiency and offers potential for extension to tasks beyond classification. The researchers [30] introduce the Dynamic-Resolution Network (DRNet), a novel solution designed to address the high computational costs associated with deploying deep Convolutional Neural Networks (CNNs) on devices with limited resources. The core premise is that the minimum resolution needed for accurate image classification varies significantly between ëasyänd "hardïnput samples, revealing redundancy in traditional fixed-resolution pipelines. To exploit this inefficiency, DRNet integrates a specialized, low-cost resolution predictor that dynamically selects the most appropriate and minimal resolution for each image instance. This approach mandates the use of resolution-aware Batch Normalization (BN) layers within the main network to effectively handle the multi-resolution inputs in an end-to-end training setting. Experimental validation on large datasets, utilizing models such as ResNet, demonstrated that implementing DRNet achieves noteworthy reductions in floating-point operations (FLOPs)—for instance, achieving a 34% reduction—while maintaining or even improving classification accuracy compared to baseline models. Yang et al. [31] propose the Resolution Adaptive Network (RANet) to optimize accuracy and computational cost by leveraging spatial redundancy. RANet uses lightweight sub-networks to process low-resolution features, allowing ëasyßamples to exit early, while higher-resolution paths handle challenging samples. Results on CIFAR-10/100 and ImageNet show superior efficiency, matching MSDNet with about 27% fewer FLOPs on ImageNet. The Scale Boosting Model (SBM) was introduced by [32] to facilitate efficient deep learning for remote sensing scene classification in computationally constrained on-orbit environments by implementing adaptive inference. This dynamic approach incrementally builds scale learners in a scale-increasing manner, achieving adaptive allocation of computational parameters through confidence-based early exiting. Validation across three benchmark datasets demonstrated superior classification accuracy and significantly reduced computational resource consumption (FLOPs). El Houby [33] proposes a transfer-learning framework employing VGG19 and EfficientNetB0 to identify COVID-19 from chest X-rays within the COVID-19 Radiography Database, assessing various image-enhancement methods and lung segmentation techniques. The results show that enhancement, especially CLAHE applied to full images, makes performance much better in both binary and four-class settings. Hussein et al. [34] propose a Custom-CNN model with eight weighted layers, incorporating dropout and batch normalization to automatically classify chest X-rays into COVID-19, normal, and pneumonia categories, achieving high accuracy despite a limited dataset size. We evaluate EACS across two medical imaging modalities—CT scans and chest X-rays (CXR)—using benchmark datasets: NIH ChestX-ray14, COVID-19 Radiography Database, and COVID-19 CT Scan Dataset. These datasets offer diverse pathology coverage, high clinical realism, and expert-level annotations. Experimental results show that EACS improves model robustness and adaptability under variable image complexity, all while maintaining practical computational efficiency for clinical deployment. EfficientNet-B0 serves as the baseline model for this study. Developed through neural architecture search (NAS) on the MobileNetV2 backbone, EfficientNet-B0 prioritizes both accuracy and computational efficiency. Unlike traditional CNNs that scale depth, width, or resolution independently, EfficientNet employs a compound scaling strategy that uniformly scales all three dimensions using a single coefficient. This balanced design enables higher classification accuracy with significantly fewer parameters and FLOPs compared to conventional models such as ResNet and VGG. Furthermore, its modular architecture allows seamless scaling to deeper and wider variants (EfficientNet-B1 to B7) without redesigning the network, making B0 an ideal choice for evaluating the impact of the proposed EACS mechanism.

3. Materials and methods

This section outlines the datasets, pre-processing pipeline, and the proposed Entropy-Aware Compound Scaling (EACS) framework developed for adaptive classification of chest X-ray (CXR) and computed tomography (CT) images. The methodology is structured to: (i) describe the datasets and their sources for both imaging modalities, (ii) present the pre-processing steps applied to ensure balanced and well-organized data suitable for model training, (iii) detail the design and integration of the EACS model with the EfficientNet architecture for handling both binary and multi-class classification tasks, and (iv) explain the training configurations employed to evaluate the proposed approach.

3.1 Data description

This study employs publicly available and clinically validated datasets to evaluate the proposed method in both multi-class and binary classification tasks using two distinct imaging modalities: chest X-ray (CXR) and computed tomography (CT). For the CXR modality, the primary source is the NIH ChestX-ray14 dataset [35], which contains 112,120 frontal-view chest radiographs labeled for 14 thoracic diseases. In this work, thirteen categories were retained: Atelectasis, Cardiomegaly, Consolidation, Edema, Effusion, Emphysema, Fibrosis, Infiltration, Mass, Nodule, Pleural Thickening, Pneumonia, and Pneumothorax. To these categories, two additional classes, COVID-19 and Normal, were added from the COVID-19 Radiography Database [36]. The COVID-19 class was included to represent novel and severe lung infections, while the Normal class provided healthy lung samples, enabling the model to distinguish between pathological and non-pathological CXR images. This expansion resulted in a total of 15 CXR categories. For the CT modality, the COVID-19 CT Scans dataset [37, 38] was used, containing two categories: COVID-19 and Normal. This dataset was incorporated to evaluate the proposed model's performance in a different imaging modality and to assess cross-modality generalization. For both modalities, 500 images were randomly selected for each class when more than 500 samples were available, ensuring balanced class distributions for training and evaluation as listed in Table 1.

3.2 Data pre-processing

In the original NIH ChestX-ray14 dataset [35], all CXR images are stored in a single directory, and labels are provided in a metadata file. Many images are labeled with multiple diseases, which can introduce label noise in a single-label classification framework; therefore, all multi-label images were excluded. The remaining single-disease images were organized into separate, disease-specific directories using custom MATLAB scripts. For the CXR modality, the 13 retained NIH disease categories were each reduced to a balanced subset of 500 images, where possible, through random sampling, and the two additional CXR categories, COVID-19 and Normal, were also balanced to 500 images

Table 1. Summarizes all classes and their corresponding image counts from the three datasets.

Dataset source	Class label	No. of images
NIH ChestX-ray14 (CXR) [35]	Atelectasis, Consolidation, Infiltration, Pneumothorax, Edema, Emphysema, Fibrosis, Effusion, Pneumonia, Pleural thickening, Cardiomegaly, Nodule Mass.	500 / Class
COVID-19 Radiography chest x-ray [36]	Covid-19, Normal	
COVID-19 CT scans (CT) [37]	Covid-19, Healthy	

each, sampled from the COVID-19 Radiography Database [36]. For the CT modality, pre-processing involved selecting 500 images each for COVID-19 and Normal from the COVID-19 CT Scans dataset [37], and since this dataset is binary and already modality-specific, no multi-label exclusion was necessary. This pre-processing produced two balanced datasets: a CXR dataset containing 15 categories (13 NIH thoracic diseases plus COVID-19 and Normal), each with 500 images, and a CT dataset containing 2 categories (COVID-19 and Normal), each with 500 images. This separation ensures that the model can be trained and evaluated on each modality independently, enabling a direct comparison of performance between CXR and CT imaging. All images from both modalities were resized to 224×224 and normalized to the [0,1] range without any augmentation. The models were trained using the Adam optimizer (learning rate = 0.001, β_1 = 0.9, β_2 = 0.999), with a batch size of 16 and either categorical or binary cross-entropy, depending on whether the task was multi-classification or binary. The training was conducted for a total of 20 epochs under identical conditions for both the baseline and EACS-enhanced models.

3.3 Proposed model: Entropy-aware compound scaling (EACS)

EfficientNet's compound scaling strategy offers a unified and computationally elegant method for scaling model depth, width, and resolution. However, it assumes uniform visual complexity across all input images, which is often unrealistic in medical imaging applications. Clinical datasets—such as chest X-rays (CXR) and CT scans—exhibit high intra-class variability due to differences in acquisition protocols, pathological features, and anatomical structures. Such heterogeneity necessitates a more adaptive, input-sensitive scaling mechanism. To address this limitation, we propose Entropy-Aware Compound Scaling (EACS) a novel extension of compound scaling that adjusts model capacity based on the inherent complexity of each input image. EACS leverages Shannon entropy as a statistical proxy for image complexity, quantifying the structural richness or uncertainty in each sample. For each input image x, Shannon entropy was computed using the full image region (no cropping or patch subdivision). All chest X-ray and CT images were processed as 8-bit grayscale, yielding L=256 intensity levels. A histogram h(i) of pixel intensities was computed over the entire 224×224 image and converted to a discrete probability distribution, Eq. 1.

$$p(i) = \frac{h(i)}{\sum_{j=0}^{L-1} h(j)}; \quad Where \;\; i \in [0, L-1] \tag{1}$$

Shannon entropy was then computed as in Eq. 2:

$$H(x) = -\sum_{i=0}^{L-1} p(i) \times \log_2 p(i) \tag{2}$$

To compare entropy values across images and ensure bounded compatibility with the scaling factor in EACS, the entropy was normalized to the range[0,1]. Because the maximum entropy of an 8-bit grayscale image is, Eq. 3:

$$H_{max} = \log_2 256 = 8 Bits \tag{3}$$

the normalized entropy is defined as, Eq. 4:

$$Entropy_{norm}(x) = \frac{H(x)}{8} \tag{4}$$

This normalized entropy provides a consistent measure of image complexity, where low-texture or uniform images yield values near 0, and structurally rich images yield values closer to 1. High-entropy images, characterized by overlapping anatomical regions or complex textures, demand greater model capacity. In contrast, low-entropy images, with clearly defined structures, can be accurately classified using fewer parameters, thereby reducing computational overhead. EACS modifies the original compound scaling coefficient φ using the following entropy-adjusted formula, Eq. 5:

$$\varphi'(x) = \varphi(1 + \eta \times Entropy_{norm}) \tag{5}$$

where η is a tunable sensitivity parameter and Entropynorm represents the normalized image entropy within the range [0, 1]. The adjusted coefficient φ' is then applied to the scaling dimensions of EfficientNet as follows, Eq. 6:

$$d = \alpha^{\varphi'}, \omega = \beta^{\varphi'}, r = \gamma^{\varphi'} \qquad Subjected \;\; to \;\; \alpha \times \beta^2 \times \gamma^2 \approx 2 \tag{6}$$

Where $\alpha, \beta, \gamma > 1$. In this instance, φ is the compound scaling coefficient, while α, β, and γ are the scaling constants utilized by EfficientNet to uniformly adjust the model's capacity across three dimensions: α controls the number of layers within the network and its depth, β controls the number of channels per layer in the network, hence increasing its width, and gcd regulates the extent to which the resolution of the input image varies. These constants maintain a balanced scaling ratio, ensuring that the model expands uniformly in all directions without excessively increasing computational costs. From a theoretical perspective, this adaptive scaling aligns with the gradient behaviour of the cross-entropy loss function. High-entropy samples tend to produce smaller gradients $\partial l / \partial \varphi'$, which benefit from increased model capacity to accelerate convergence. By dynamically linking model complexity to image content, EACS enhances learning efficiency, reduces overfitting, and enhances classification accuracy—particularly in high-stakes, resource-constrained medical diagnostic applications. The proposed EACS method is implemented as a complete framework for adaptive medical image classification, integrating both pre-processing and model scaling in a unified pipeline. As illustrated in Fig. 1, the framework begins with the input image (CXR or CT), computes and normalizes Shannon entropy, and adaptively determines the scaling coefficient according to the measured image complexity.

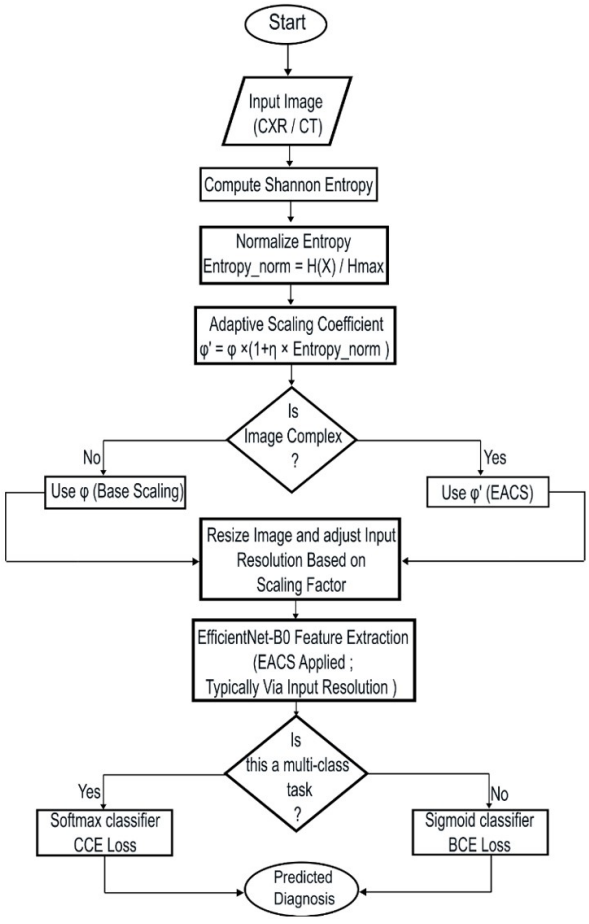

Figure 1. Workflow of the proposed entropy of compound scaling (EACS).

Depending on the complexity level, either the base scaling factor φ or the entropy-adjusted scaling factor φ' is applied. The input image is then resized and its resolution adjusted according to the selected scaling factor before being processed by the EfficientNet-B0 backbone for feature extraction. Finally, a classification head is chosen based on the task type, with a softmax classifier and categorical cross-entropy (CCE) loss for multi-class tasks, or a sigmoid classifier and binary cross-entropy (BCE) loss for binary tasks. This end-to-end design ensures that computational resources are adaptively allocated to each sample, thereby improving efficiency while maintaining high diagnostic accuracy across both imaging modalities.

3.4 Training procedure

All experiments were conducted on a personal laptop equipped with an Intel *Core*^{TM} i7-10750H CPU operating at 2.60 GHz, 8 GB RAM, and a 4 GB GPU, running a 64-bit Windows operating system. The datasets were divided into training and testing subsets using a 70:30 split to evaluate model generalization across both the multi-class CXR task and the binary CT task. Prior to training, all images were resized to 224×224 pixels to match EfficientNet's input requirements, and no data augmentation was applied to preserve the clinical integrity of the medical images. For the CXR multi-class task, the model was trained for up to 40 epochs with a batch size of 16–32, employing early stopping to prevent overfitting, whereas for the CT binary classification task, convergence was typically achieved within 40 epochs using a batch size of 32. An initial learning rate of $1/10^4$ was used for both datasets, with a reduced rate of $5/10^5$ optionally explored for CT scans to enhance stability. The Categorical Cross-Entropy (CCE) loss function was applied for the multi-class classification, while Binary Cross-Entropy (BCE) was used for the binary task, and the Adam optimizer was selected for its adaptability to sparse gradients and compatibility with the entropy-aware compound scaling strategy, ensuring efficient convergence across both imaging modalities. While the flowchart in Fig. 1 provides a high-level overview of the EACS framework, it does not capture the exact operational steps required for implementation. To ensure reproducibility and facilitate future research, the proposed approach is formalized in Algorithm 1 as shown in Fig. 2, which outlines the complete training pipeline in pseudocode form.

Algorithm 1 Entropy-Aware EfficientNet Training for X-ray , CT Modalities

Require: Dataset $\mathcal{D} = \{(X_i, y_i)\}_{i=1}^{N}$, base scaling factor ϕ, entropy hyperparameter η, number of classes C
Ensure: Trained EfficientNet model $\mathcal{F}$
for each epoch $e = 1$ to E **do**
  for each image X_i in dataset $\mathcal{D}$ **do**
    Compute pixel histogram of X_i
    Calculate Shannon entropy:

$$H(X_i) = -\sum_j p(x_j) \log_2 p(x_j)$$

    Normalize entropy: EntropyNorm $\leftarrow \frac{H(X_i)}{H_{\max}}$
    Compute adaptive scaling coefficient:

$$\phi' = \phi \cdot (1 + \eta \cdot \text{EntropyNorm})$$

    Adjust model parameters using ϕ': depth, width, resolution
    Resize X_i and forward it through EfficientNet to get prediction $\hat{y}_i$
    if X_i is chest X-ray **then**
      Apply softmax to output
      Compute categorical cross-entropy loss:

$$\mathcal{L}_i = -\sum_{c=1}^{C} y_i^{(c)} \log(\hat{y}_i^{(c)})$$

    else
      Apply sigmoid to output
      Compute binary cross-entropy loss:

$$\mathcal{L}_i = -[y_i \log(\hat{y}_i) + (1 - y_i) \log(1 - \hat{y}_i)]$$

    end if
    Update model $\mathcal{F}$ using backpropagation
  end for
end for
return Trained model $\mathcal{F}$

Figure 2. Pseudocode for EACS (Proposed Model).

4. Results and discussion

This section presents the experimental results for the proposed Entropy-Aware Compound Scaling (EACS) approach, evaluated across two medical imaging modalities: chest X-ray (CXR) and computed tomography (CT). For each dataset, the first step by reporting the baseline performance of the EfficientNet-B0 model without adaptive scaling; moreover, the second step is implemented by enhancing the results obtained after integrating EACS, as shown in Fig. 3.

4.1 Chest X-ray dataset

4.1.1 Baseline model performance analysis

The baseline EfficientNet-B0 model was evaluated on a chest X-ray dataset containing 15 diagnostic categories, covering both common and rare thoracic conditions. The model delivered strong overall classification performance, achieving 88.07% overall accuracy, 98.41% per-class average accuracy, and 98.39% weighted accuracy. Such results indicate that even without adaptive mechanisms, the network is capable of consistently distinguishing between a wide range of pathologies. The confusion matrix revealed pronounced diagonal dominance, particularly for categories with well-defined radiographic signatures. For example, Covid-19, Mass, Normal, and Pneumothorax achieved ≥ 134 correct predictions out of 140, underscoring the model's effectiveness in detecting diseases with distinctive structural patterns. However, the analysis also exposed systematic weaknesses. Certain conditions with overlapping visual characteristics were frequently misclassified. Cardiomegaly was often mistaken for Consolidation or Edema—both of which can present similar silhouettes in chest radiographs—while Pleural Thickening was confused with Nodule or Pneumonia, likely due to subtle pleural boundary changes that are challenging to differentiate. These patterns were further reflected in the ROC-AUC scores, where all categories exceeded 0.92 but performance for Nodule (0.9272) and Consolidation (0.9292) lagged behind. These relatively lower values suggest reduced discriminative power for conditions with diffuse or subtle manifestations. Taken together, these findings illustrate that while the baseline EfficientNet-B0 offers a robust starting point for automated chest X-ray classification, its fixed-scaling architecture limits its adaptability to cases of high visual similarity, leaving room for methods that can dynamically allocate computational resources based on image complexity.

4.1.2 Enhanced performance with Entropy-aware scaling

The integration of the proposed Entropy-Aware Compound Scaling (EACS) mechanism produced measurable and consistent improvements across all evaluation metrics. Compared to the baseline, the overall accuracy increased to 90.94%, while both per-class and weighted accuracies rose to 98.79%. This gain can be attributed to EACS's ability to dynamically adjust network depth, width, and resolution in direct response to the entropy of the input image, ensuring that diagnostically complex cases receive the additional representational capacity they require. This adaptive behavior was clearly reflected in the confusion matrix, which exhibited a denser diagonal distribution than the baseline. Most categories exceeded 136 correct predictions out of 140, indicating greater precision and reduced misclassification rates. Notably, classes that had been problematic for the baseline model—such as Cardiomegaly, Pleural Thickening, and Nodule—showed markedly improved separability from visually similar categories. This suggests that the entropy-guided scaling mechanism effectively refines decision boundaries in challenging diagnostic scenarios. The ROC-AUC analysis reinforced these observations, with all classes surpassing 0.948. Significant gains were recorded for Normal (0.9559), Edema (0.9545), and Covid-19 (0.9540), while the baseline's weakest categories, Consolidation and Nodule, improved to 0.9489 and 0.9499, respectively. These results highlight more than just an incremental performance boost—they demonstrate the practical impact of embedding a mathematical scaling strategy directly into the model's architecture. By linking model capacity to the intrinsic complexity of each image, EACS achieves a balance between computational efficiency and diagnostic accuracy, addressing a long-standing challenge in medical image analysis. In doing so, it lays a foundation for future AI diagnostic systems that can scale intelligently across heterogeneous medical datasets, ensuring robust performance even in the most visually ambiguous cases.

4.1.3 Comparative performance summary

The comparative results between the baseline and EACS-enhanced models highlight the practical benefits of adaptive scaling in chest X-ray analysis. EACS yielded a +2.87% improvement in overall accuracy, a +0.38% gain in both per-class and weighted accuracies, and raised the lowest ROC-AUC from 0.9272 to 0.9489. The highest ROC-AUC also improved, from 0.9460 to 0.9559. These gains are not only statistically significant but also clinically relevant, as they enhance the model's reliability in differentiating ambiguous

cases—a critical requirement for AI-assisted diagnostic workflows. The summarized metrics are presented in Table 2, while Fig. 4 shows the corresponding confusion matrices and ROC curves for chest X-ray images before and after applying EACS, clearly illustrating the model's performance gains across all diagnostic classes.

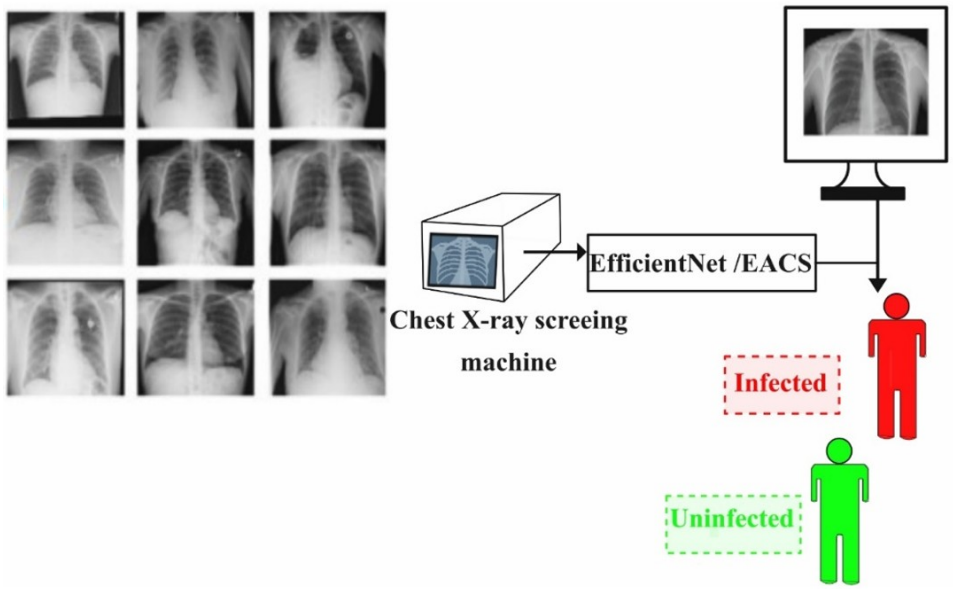

Figure 3. Sample chest X-ray images with Automated identification using EfficientNet/EACS (proposed model).

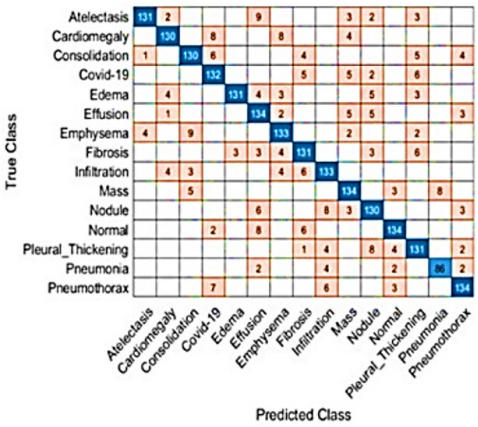

(a) Confusion matrix of the baseline model

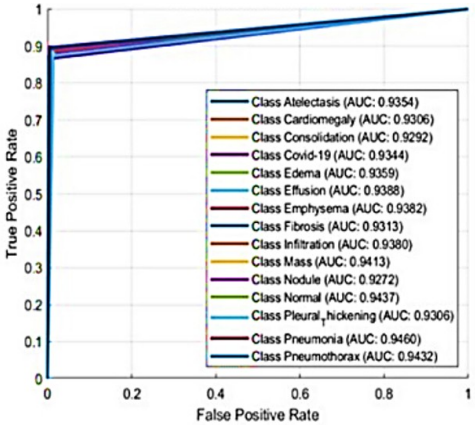

(b) ROC curves and AUC of Fig 4a

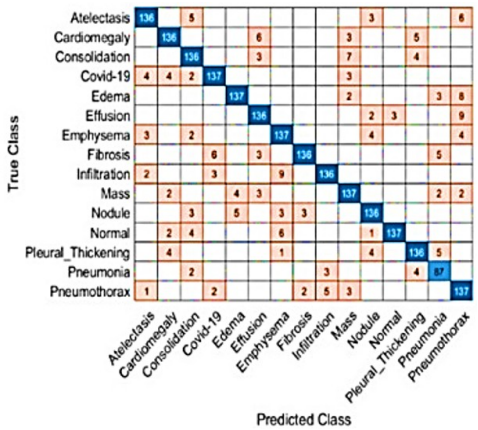

(c) confusion matrix of the EACS

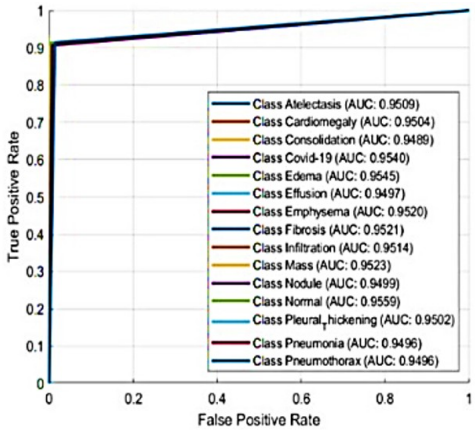

(d) ROC curves and AUC of Fig 4c

Figure 4. (a) Confusion matrix of the baseline model on the Chest X-ray dataset; (b) ROC curves and AUC values for the baseline model; (c) confusion matrix of the EACS; and (d) ROC curves and AUC values for the EACS on the Chest X-ray dataset.

Table 2. Comparative classification metrics for chest X-ray dataset before and after EACS application.

Metric	Baseline (EfficientNet-B0)	After EACS
Overall accuracy (%)	88.07	90.94
Per-class average accuracy (%)	98.41	98.79
Weighted accuracy (%)	98.39	98.79
AUC range	0.9272 – 0.9460	0.9489 – 0.9559
Lowest performing class (AUC)	Nodule (0.9272)	Nodule (0.9499)
Highest performing class (AUC)	Pneumonia (0.9460)	Normal (0.9559)

4.2 CT-scan dataset

Figure 5 presents representative CT scan segments that show a range of pulmonary abnormalities relevant to COVID-19 inspection. The diagram on the right shows the automated process where CT-Scan images are sent to the EfficientNet/EACS model for extracting features and categorizing them. The system distinguishes between COVID-19 and Healthy cases using advanced scaling techniques that improve speed and accuracy in computer-aided diagnosis directly from CT scan images.

4.2.1 Baseline model performance analysis

When applied to the CT scan dataset—comprising two diagnostic categories, COVID-19 and Healthy—the baseline EfficientNet-B0 model demonstrated robust binary classification capability. Achieving an overall accuracy of 88.67%, with per-class average and weighted accuracies matching this figure, the model showed balanced performance across the two classes. Out of 300 total samples, it correctly identified 132 COVID-19 and 134 Healthy cases, yielding 266 accurate predictions in total. A closer examination of class-wise metrics reveals precision, recall, and F1-score values that are nearly balanced across the two categories. COVID-19 cases recorded a precision of 89.19%, recall of 88.00%, and F1-score of 88.59%, while Healthy cases achieved 88.16% precision, 89.33% recall, and 88.74% F1-score. Both categories shared an identical ROC-AUC score of 0.8867, reflecting a solid level of discriminative capability. However, the presence of 34 misclassifications—18 Healthy cases labeled as COVID-19 and 16 COVID-19 cases labeled Healthy—highlights the challenge of differentiating between early-stage or atypical infections and normal pulmonary structures. Such errors are likely influenced by mild or ambiguous CT patterns and inter-slice variability, where disease manifestations are either too subtle or closely resemble healthy tissue. These limitations emphasize the potential value of adaptive modeling strategies capable of tailoring network complexity to input difficulty.

4.2.2 Enhanced performance with entropy-aware scaling

Building upon the baseline analysis, the integration of Entropy-Aware Compound Scaling (EACS) into the EfficientNet-B0 architecture led to clear and consistent performance gains. By dynamically modulating network depth, width, and resolution in response to input complexity, EACS improved both precision and robustness in CT-based COVID-19 detection. The model's overall accuracy rose to 91.67%, with per-class and weighted accuracies also reaching 91.67%. Misclassification rates dropped significantly, with 137 COVID-19 and 138 Healthy cases correctly identified, resulting in only 13 false positives and 12 false negatives. This represents an improvement of nine additional correct predictions compared to the baseline. Class-wise, COVID-19 predictions achieved a precision of 91.95%, recall of 91.33%, and F1-score of 91.64%, while Healthy cases attained 91.39% precision, 92.00% recall, and 91.69% F1-score. The ROC-AUC for both classes improved to 0.9167, indicating greater confidence in decision boundaries and earlier separation between positive and negative cases—an essential factor for rapid clinical screening. These results highlight how EACS addresses the inherent challenge of visually similar CT patterns. By assigning greater representational capacity to higher-entropy, diagnostically complex inputs, the approach mitigates the ambiguity that often plagues pulmonary imaging interpretation.

4.2.3 Comparative performance summary CT-scan dataset

The side-by-side comparison between baseline and EACS-enhanced performance on the CT-Scan dataset underscores the tangible benefits of adaptive scaling. While the baseline model achieved solid accuracy (88.67%) and identical AUC values of 0.8867 for both categories, its 34 misclassifications and moderate F1-scores left room for improvement—especially in borderline or ambiguous cases. With EACS, the model's overall accuracy improved by 3 percentage points to 91.67%, misclassifications decreased to 25, and both precision and recall saw measurable gains. The ROC-AUC improvement to 0.9167 reflects not just statistical gains but also enhanced clinical reliability, enabling more confident classification in scenarios where early detection is critical. The key classification metrics for the CT-Scan dataset are summarized in Table 3, and the corresponding confusion matrices and ROC curves in Fig. 6 visually demonstrate the performance improvements achieved with EACS across both diagnostic categories.

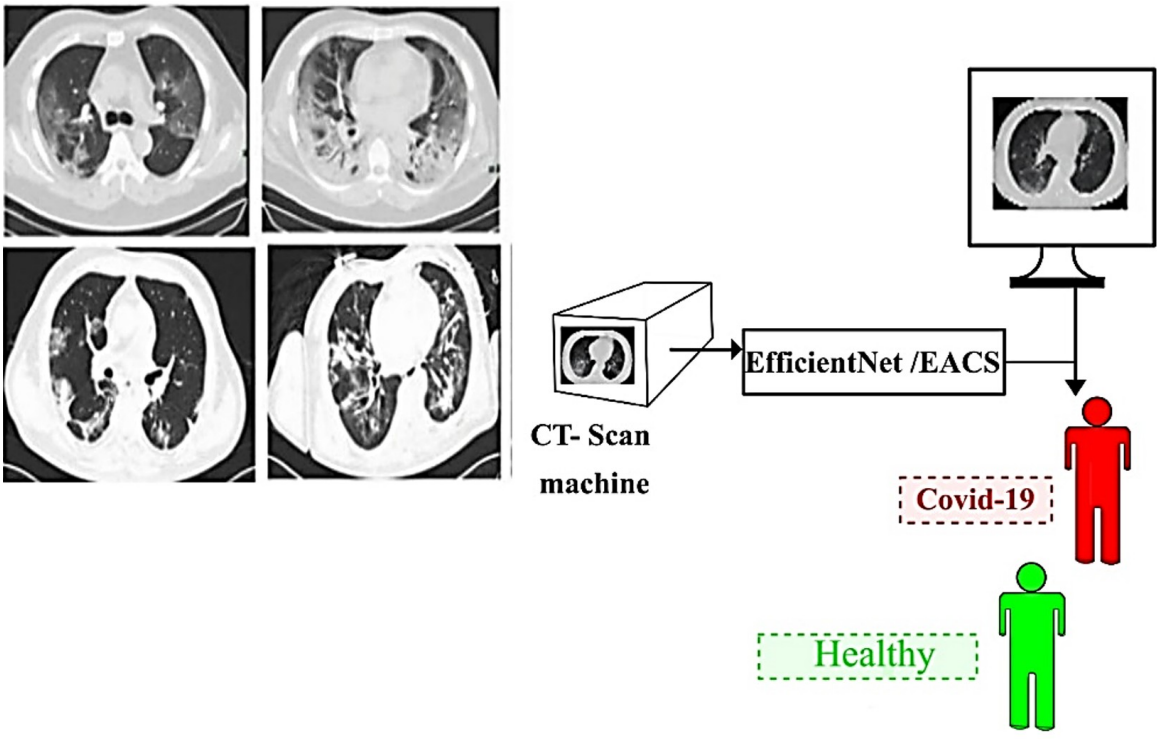

Figure 5. Sample chest X-ray images with automated identification using efficientNet/EACS (proposed model).

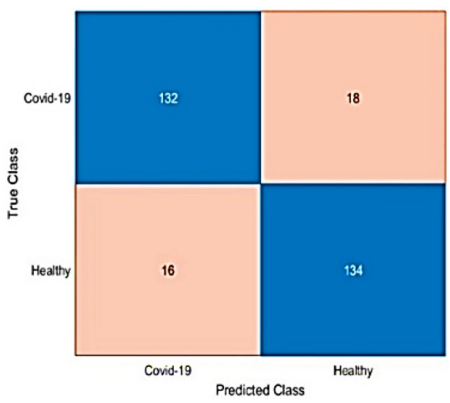

(a) Confusion matrix of the baseline

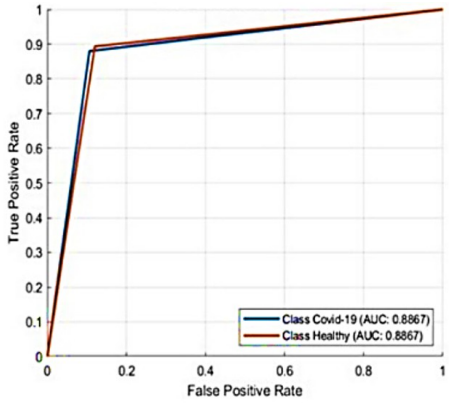

(b) ROC and AUC values of Fig. 6a

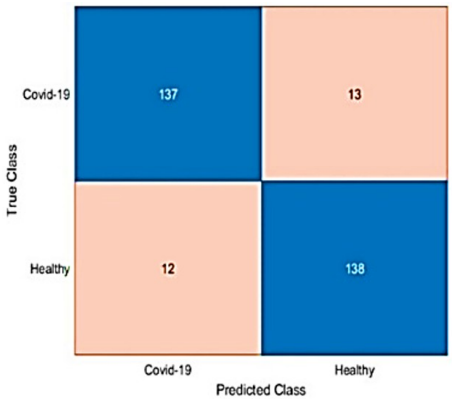

(c) confusion matrix of the EACS

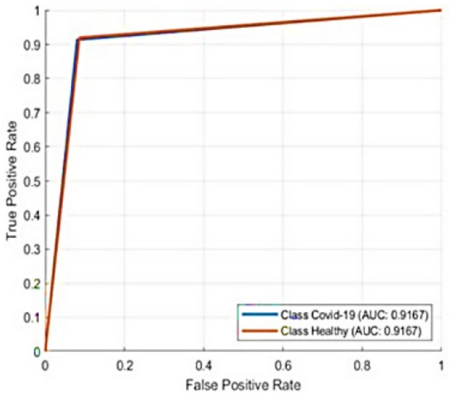

(d) ROC and AUC values of Fig. 6c

Figure 6. (a) Confusion matrix of the baseline model on the CT-scan dataset; (b) ROC curves and AUC values for the baseline model; (c) confusion matrix of the EACS; and (d) ROC curves and AUC values for the EACS on the CT-scan dataset.

Table 3. Comparative classification performance of the baseline EfficientNet-B0 model and its (EACS) counterpart on the CT-Scan.

Metric	Baseline (EfficientNet-B0)	After EACS
Overall accuracy (%)	88.67	91.67
Per-class average Accuracy (%)	88.67	91.67
Weighted accuracy (%)	88.67	91.67
Total correct predictions	266.0	275.0
Total misclassifications	34.00	25.00

Notably, the relative improvement achieved with EACS was slightly higher for CT-Scans than for chest X-rays. This suggests that the proposed scaling strategy demonstrates particularly strong adaptation in binary classification settings, where subtle anatomical differences exert a critical influence on diagnostic accuracy. Recent studies demonstrate the importance of enhancing the convolutional neural network (CNN) for detecting COVID-19. Compared with previous COVID-19-focused works using EfficientNet variants, the proposed EACS method demonstrates better flexibility and broader applicability:

- A 3D EfficientNet-B0 based model had limited performance, with an AUC of 0.681, when used for analysing lungs [39].
- A dual-sensor system for detecting COVID-19 with EfficientNet-B0 achieved 82% accuracy, making it the best single model [40].

The proposed Entropy-aware Compound Scaling (EACS) enhanced EfficientNet-B0 achieves 90.94% accuracy in CXR and 91.67% accuracy in CT scans, exceeding performance levels in existing literature These comparisons point out EACS as a unique and innovative mathematical approach that enhances COVID-19 detection across various methods.

4.3 Evaluation metrics

To assess the performance of the baseline and proposed models, the mathematical approach for the proposed model is based on the following equations derived from previous studies [41–43].

- Accuracy is defined as the number of correctly categorized predictions by a model compared to the total number of classified examples and can be calculated using Eq. 7:

$$Accuracy = \frac{TP+TN}{TP+TN+FP+FN} \tag{7}$$

- Precision indicates how many of the predicted positives are actually correct. It is defined as, Eq. 8:

$$Precision = \frac{TP}{TP+FP} \tag{8}$$

- Recall (Sensitivity) refers to the accuracy of true positive predictions for occurrences that belong to the positive class, Eq. 9.

$$Recall = \frac{TP}{TP+FN} \tag{9}$$

- Recall refers to the accuracy of true positive predictions for occurrences that belong to the positive class, Eq. 10.

$$Specificity = \frac{TN}{TN+FP} \tag{10}$$

- F-1 Score: Balances precision and recall, especially useful for imbalanced datasets, Eq. 11.

$$F1 = 2 \times \frac{Precision \times Recall}{Precision + Recall} \tag{11}$$

- AUC represents the model's ability to discriminate between classes, Eq. 12.

$$AUC = \int_0^1 TPR(x)dx \tag{12}$$

- Error Rate: Represents the proportion of incorrect predictions, Eq. 13.

$$Error\_Rate = 1 - Accuracy \tag{13}$$

These metrics were applied to both chest X-ray and CT scan datasets for the baseline EfficientNet-B0 and EACS-enhanced models. As shown in Fig. 7, EACS consistently outperformed the baseline across all metrics, confirming its adaptability to varying image complexities and its effectiveness in improving diagnostic reliability.

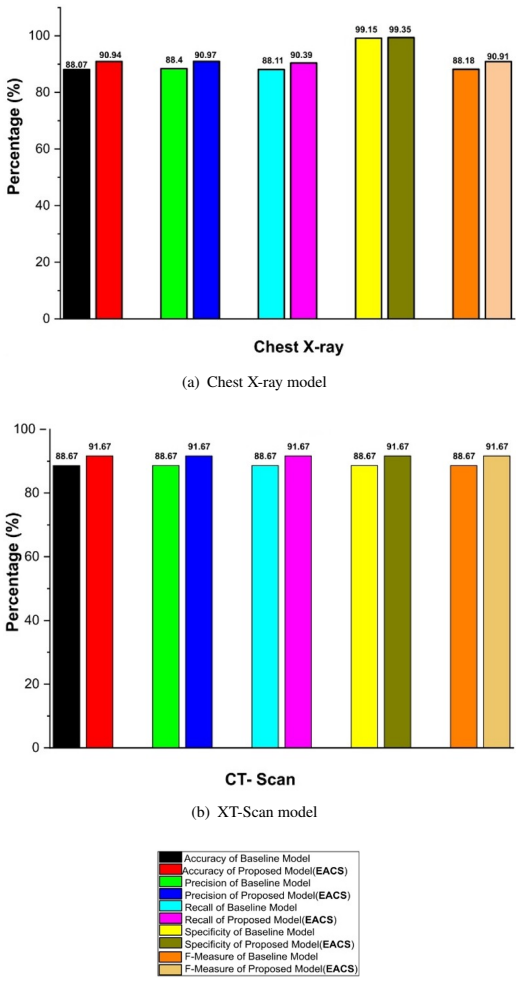

(a) Chest X-ray model

(b) XT-Scan model

Figure 7. Comparison of performance metrics between the baseline model and the proposed EACS model for (a) Chest X-ray and (b) CT-scan images.

5. Conclusion and future work

This study introduced an entropy-aware compound scaling strategy to enhance the accuracy and adaptability of EfficientNet-B0 in medical image classification tasks. By integrating normalized Shannon entropy as a dynamic scaling factor, the model adjusts its capacity based on the visual complexity of each image, leading to more efficient and effective learning. Experimental results on both chest X-ray and CT scan datasets confirmed the benefits of this approach. For chest X-rays, the overall accuracy improved from 88.07% to 90.94%, with a corresponding reduction in error rate from 0.1193 to 0.0906. Similarly, for CT-Scans, accuracy increased from 88.67% to 91.67%, while the error rate decreased from 0.1133 to 0.0833. These improvements demonstrate the method's ability to dynamically allocate computational resources, thereby enhancing diagnostic reliability across imaging modalities. Future work will explore extending this approach to alternative architectures, such as Vision Transformers, to evaluate its generalizability and scalability.

Authors' contribution

All authors contributed equally to the preparation of this article.

Declaration of competing interest

To ensure the quality and clarity of our manuscript, we used Grammarly to check grammatical and typo errors. Additionally, we used AI tools to enhance the readability of the text, ensuring that our findings were presented in a clear and acceptable manner.

Funding source

This study didn't receive any specific funds.

Data availability

The data that support the findings of this study are available from the corresponding author upon reasonable request.

REFERENCES

[1] NIEHS-community, "Lung diseases," *National Institute of Environmental Health Sciences, Health & Education*. [Online]. Available: https://www.niehs.nih.gov/

[2] S. Rana, M. J. Hosen, T. J. Tonni, M. A. H. Rony, K. Fatema, M. Z. Hasan, M. T. Rahman, R. T. Khan, T. Jan, and M. Whaiduzzaman, "Deepchestgnn: A comprehensive framework for enhanced lung disease identification through advanced graphical deep features," *Sensors*, vol. 24, no. 9, 2024. [Online]. Available: https://doi.org/10.3390/s24092830

[3] I. Arevalo-Rodriguez, D. Buitrago-Garcia, D. Simancas-Racines, P. Zambrano-Achig, R. D. Campo, A. Ciapponi, O. Sued, L. Martínez-García, A. Rutjes, N. Low, P. M. Bossuyt, J. A. Perez-Molina, and J. Zamora, "False-negative results of initial rt-pcr assays for covid-19: A systematic review," *medRxiv*, 2020. [Online]. Available: https://www.medrxiv.org/content/early/2020/08/13/2020.04.16.20066787

[4] C. Huang, Y. Wang, X. Li, L. Ren, J. Zhao, Y. Hu, L. Zhang, G. Fan, J. Xu, X. Gu, Z. Cheng, T. Yu, J. Xia, Y. Wei, W. Wu, X. Xie, W. Yin, H. Li, M. Liu, Y. Xiao, H. Gao, L. Guo, J. Xie, G. Wang, R. Jiang, Z. Gao, Q. Jin, J. Wang, and B. Cao, "Clinical features of patients infected with 2019 novel coronavirus in wuhan, china," *The Lancet*, vol. 395, no. 10223, pp. 497–506, 2020. [Online]. Available: https://doi.org/10.1016/S0140-6736(20)30183-5

[5] J. Pang, M. X. Wang, I. Y. H. Ang, S. H. X. Tan, R. F. Lewis, J. I.-P. Chen, R. A. Gutierrez, S. X. W. Gwee, P. E. Y. Chua, Q. Yang, X. Y. Ng, R. K. Yap, H. Y. Tan, Y. Y. Teo, C. C. Tan, A. R. Cook, J. C.-H. Yap, and L. Y. Hsu, "Potential rapid diagnostics, vaccine and therapeutics for 2019 novel coronavirus (2019-ncov): A systematic review," *Journal of Clinical Medicine*, vol. 9, no. 3, 2020. [Online]. Available: https://doi.org/10.3390/jcm9030623

[6] S. A. Meo, A. Am, T. Al-khlaiwi, I. M. U. Meo, D. M. Halepoto, M. Iqbal, A. M. Usmani, W. M. Hajjar, and N. Ahmed, "Novel coronavirus 2019-ncov: prevalence, biological and clinical characteristics comparison with sars-cov and mers-cov." *European review for medical and pharmacological sciences*, vol. 24 4, pp. 2012–2019, 2020. [Online]. Available: https://api.semanticscholar.org/CorpusID:212567658

[7] WHO-Team, "Coronavirus disease 2019 (covid-19) situation report 51," *World Health Organization*, 2020. [Online]. Available: https://who18.createsend.com/campaigns/reports/viewCampaign.aspx?d=j&c=99FA4938D049E3A8&ID=71A4C8A1A112FCB72540EF23F30FEDED&temp=False&tx=0&source=Report

[8] WHO-team, "Weekly operational update on covid-19 - 16 october 2020," *World Health Organization*, 2020. [Online]. Available: https://www.who.int/publications/m/item/weekly-update-on-covid-19---16-october-2020

[9] L. Alzubaidi, J. Zhang, A. J. Humaidi, A. Al-Dujaili, Y. Duan, O. Al-Shamma, J. Santamaría, M. A. Fadhel, M. Al-Amidie, and L. Farhan, "Review of deep learning: concepts, cnn architectures, challenges, applications, future directions," *Journal of Big Data*, vol. 8, no. 1, p. 53, 2021. [Online]. Available: https://doi.org/10.1186/s40537-021-00444-8

[10] Y. LeCun, Y. Bengio, and G. Hinton, "Deep learning," *nature*, vol. 521, no. 7553, pp. 436–444, 2015. [Online]. Available: https://doi.org/10.1038/nature14539

[11] S. Takahashi, Y. Sakaguchi, N. Kouno, K. Takasawa, K. Ishizu, Y. Akagi, R. Aoyama, N. Teraya, N. Shinkai, H. Machino, K. Kobayashi, K. Asada, M. Komatsu, S. Kaneko, M. Sugiyama, and R. Hamamoto, "Comparison of vision transformers and convolutional neural networks in medical image analysis: A systematic review," *Journal*

of Medical Systems, vol. 48, p. 84, 09 2024. [Online]. Available: https://doi.org/10.1007/s10916-024-02105-8

[12] G. Kourounis, A. A. Elmahmudi, B. Thomson, J. Hunter, H. Ugail, and C. Wilson, "Computer image analysis with artificial intelligence: a practical introduction to convolutional neural networks for medical professionals," *Postgraduate Medical Journal*, vol. 99, no. 1178, pp. 1287–1294, 10 2023. [Online]. Available: https://doi.org/10.1093/postmj/qgad095

[13] M. Shafiq and Z. Gu, "Deep residual learning for image recognition: A survey," *Applied Sciences*, vol. 12, no. 18, 2022. [Online]. Available: https://doi.org/10.3390/app12188972

[14] X. Li, W. Zhang, and Q. Ding, "Residual neural network-based fault diagnosis of rotating machinery," *IEEE*, 2017. [Online]. Available: https://doi.org/10.1109/ICCWAMTIP.2017.8301487

[15] A. Howard, M. Sandler, B. Chen, W. Wang, L.-C. Chen, M. Tan, G. Chu, V. Vasudevan, Y. Zhu, R. Pang, H. Adam, and Q. Le, "Searching for mobilenetv3," *2019 IEEE/CVF International Conference on Computer Vision (ICCV)*, pp. 1314–1324, 2019. [Online]. Available: https://doi.org/10.1109/ICCV.2019.00140

[16] X. Du, Y. Sun, Y. Song, W. Chi, L. Dong, and X. Zhao, "Impact of input image resolution on deep learning performance for side-scan sonar classification: An accuracy–efficiency analysis," *Remote Sensing*, vol. 17, no. 14, 2025. [Online]. Available: https://www.mdpi.com/2072-4292/17/14/2431

[17] M. Tan and Q. Le, "Efficientnet: Rethinking model scaling for convolutional neural networks," *arXiv*, 05 2019. [Online]. Available: https://doi.org/10.48550/arXiv.1905.11946

[18] E. Buaka and M. Z. I. Moid, "Ai and medical imaging technology: evolution, impacts, and economic insights," *The Journal of Technology Transfer*, vol. 49, pp. 2260–2272, 06 2024. [Online]. Available: https://doi.org/10.1007/s10961-024-10100-x

[19] S. Jia, S. Jiang, Z. Lin, N. Li, M. Xu, and S. Yu, "A survey: Deep learning for hyperspectral image classification with few labeled samples," *Neurocomputing*, vol. 448, pp. 179–204, 2021. [Online]. Available: https://doi.org/10.1016/j.neucom.2021.03.035

[20] T. Wang, Y. Lei, Y. Fu, J. Wynne, W. Curran, T. Liu, and X. Yang, "A review on medical imaging synthesis using deep learning and its clinical applications," *Journal of Applied Clinical Medical Physics*, vol. 22, 12 2020. [Online]. Available: https://doi.org/10.1002/acm2.13121

[21] X. Wang, Y. Peng, L. Lu, Z. Lu, M. Bagheri, and R. Summers, "Chestx-ray8: Hospital-scale chest x-ray database and benchmarks on weakly-supervised classification and localization of common thorax diseases," *IEEE CVPR*, 05 2017. [Online]. Available: https://doi.org/10.1109/CVPR.2017.369

[22] Q. Guan, Y. Huang, Z. Zhong, Z. Zheng, L. Zheng, and Y. Yang, "Diagnose like a radiologist: Attention guided convolutional neural network for thorax disease classification," *arXiv*, 01 2018. [Online]. Available: https://doi.org/10.48550/arXiv.1801.09927

[23] R. Singh, M. K. Kalra, C. Nitiwarangkul, J. A. Patti, F. Homayounieh, A. Padole, P. Rao, P. Putha, V. V. Muse, A. Sharma, and S. R. Digumarthy, "Deep learning in chest radiography: Detection of findings and presence of change," *PLOS ONE*, vol. 13, no. 10, pp. 1–12, 10 2018. [Online]. Available: https://doi.org/10.1371/journal.pone.0204155

[24] M. A. Talukder, M. A. Layek, M. A. Hossain, M. A. Islam, M. N. e Alam, and M. Kazi, "Acu-net: Attention-based convolutional u-net model for segmenting brain tumors in fmri images," *DIGITAL HEALTH*, vol. 11, 2025. [Online]. Available: https://doi.org/10.1177/20552076251320288

[25] W. Wan, J. Chen, T. Li, Y. Huang, J. Tian, C. Yu, and Y. Xue, "Information entropy based feature pooling for convolutional neural networks," *2019 IEEE/CVF International Conference on Computer Vision (ICCV)*, pp. 3404–3413, 2019. [Online]. Available: https://doi.org/10.1109/ICCV.2019.00350

[26] Y. Guan, L. Zhang, J. Li, X. Xu, Y. Yan, and L. Zhang, "A lightweight entropy–curvature-based attention mechanism for meningioma segmentation in mri images," *Applied Sciences*, vol. 15, no. 6, 2025. [Online]. Available: https://www.mdpi.com/2076-3417/15/6/3401

[27] M. Jun, G. Cheng, W. Yixin, A. Xingle, G. Jiantao, Y. Ziqi, Z. Minqing, L. Xin, D. Xueyuan, C. Shucheng, W. Hao, M. Sen, Y. Xiaoyu, N. Ziwei, L. Chen, T. Lu, Z. Yuntao, Z. Qiongjie, D. Guoqiang, and H. Jian, "Covid-19 ct lung and infection segmentation dataset," *Zenodo*, Apr. 2020. [Online]. Available: https://doi.org/10.5281/zenodo.3757476

[28] D. Onah and R. Desai, "Deep brain net: An optimized deep learning model for brain tumor detection in mri images using efficientnetb0 and resnet50 with transfer learning," *arXiv*, 2025. [Online]. Available: https://arxiv.org/abs/2507.07011

[29] S. Teerapittayanon, B. McDanel, and H. T. Kung, "Branchynet: Fast inference via early exiting from deep neural networks," *arXiv*, 2017. [Online]. Available: https://arxiv.org/abs/1709.01686

[30] G. Huang, D. Chen, T. Li, F. Wu, L. van der Maaten, and K. Q. Weinberger, "Multi-scale dense networks for resource efficient image classification," *arXiv*, 2018. [Online]. Available: https://arxiv.org/abs/1703.09844

[31] Z. Wang, H. Zhang, X. Li, and J. Yang, "Glaunet: Global and local attention unit for dynamic convolution in cnns," *arXiv preprint*, vol. arXiv:2106.02898, 2021.

[32] L. Yang, Y. Han, X. Chen, S. Song, J. Dai, and G. Huang, "Resolution adaptive networks for efficient inference," *arXiv*, 2020. [Online]. Available: https://arxiv.org/abs/2003.07326

[33] K. Yang, N. Yang, and H. Tang, "Dynamic inference for on-orbit scene classification with the scale boosting model," *International Journal of Applied Earth Observation and Geoinformation*, vol. 138, p. 104447, 2025. [Online]. Available: https://doi.org/10.1016/j.jag.2025.104447

[34] E. El Houby, "Covid-19 detection from chest x-ray images using transfer learning," *Scientific Reports*, vol. 14, 05 2024.

[35] T. Brochet, J. Lapuyade-Lahorgue, S. Bougleux, M. Salaün, and S. Ruan, "Deep learning using havrda-charvat entropy for classification of pulmonary optical endomicroscopy," *IRBM*, vol. 42, no. 6, pp. 400–406, 2021. [Online]. Available: https://doi.org/10.1016/j.irbm.2021.06.006

[36] "Chest x-ray14 dataset," *National Institutes of Health (NIH)*, 2017. [Online]. Available: https://www.nih.gov/

[37] M. E. H. Chowdhury, T. Rahman, A. Khandakar, R. Mazhar, M. A. Kadir, Z. B. Mahbub, K. R. Islam, M. S. Khan, A. Iqbal, N. A. Emadi, M. B. I. Reaz, and M. T. Islam, "Can ai help in screening viral and covid-19 pneumonia?" *IEEE Access*, vol. 8, pp. 132 665–132 676, 2020.

[38] T. Rahman, A. Khandakar, Y. Qiblawey, A. Tahir, S. Kiranyaz, S. B. Abul Kashem, M. T. Islam, S. Al Maadeed, S. M. Zughaier, M. S. Khan, and M. E. Chowdhury, "Exploring the effect of image enhancement techniques on covid-19 detection using chest x-ray images," *Computers in Biology and Medicine*, vol. 132, p. 104319, 2021. [Online]. Available: https://doi.org/10.1016/j.compbiomed.2021.104319

[39] A. L. Dos Santos, M. C. L. Oliveira, E. A. Colosimo, R. H. Mak, C. C. Pinhati, S. C. Gallante, H. Martelli-Júnior, A. C. S. e Silva, and E. A. Oliveira, "Comparative performance of twelve machine learning models in predicting covid-19 mortality risk in children: a population-based retrospective cohort study in brazil," *PeerJ Computer Science*, vol. 11, p. e2916, 2025.

[40] S. Yang, S.-H. Lim, J.-H. Hong, J. S. Park, J. Kim, and H. W. Kim, "Deep learning-based lung cancer risk assessment using chest computed tomography images without pulmonary nodules 8 mm," *Translational Lung Cancer Research*, vol. 14, no. 1, 2025. [Online]. Available: https://tlcr.amegroups.org/article/view/95776

[41] A. Hussein, A. Garba Sharifai, O. Alia, L. Abualigah, K. Almotairi, S. K. M. Abujayyab, and A. Gandomi, "Auto-detection of the coronavirus disease by using deep convolutional neural networks and x-ray photographs," *Scientific Reports*, vol. 14, 01 2024.

[42] S. Alghamdi and T. Turki, "A novel interpretable deep transfer learning combining diverse learnable parameters for improved t2d prediction based on single-cell gene regulatory networks," *Scientific Reports*, vol. 14, 02 2024.

[43] S. Kordnoori, M. Sabeti, H. Mostafaei, and S. S. A. Banihashemi, "A deep learning framework for accurate covid-19 classification in ct-scan images," *Machine Learning with Applications*, vol. 19, p. 100628, 2025. [Online]. Available: https://doi.org/10.1016/j.mlwa.2025.100628

How to cite this article:
Nour H. Hammadah and Dhanesh Patel, (2026). 'Adaptive compound scaling of efficientNet via entropy estimation for chest X-ray and CT image', Al-Qadisiyah Journal for Engineering Sciences, 19(1), pp. 001-010. https://doi.org/10.30772/qjes.2026.164191.1705